Inferring Earth structure from combined measurements of rotational and translational ground motions

Moritz Bernauer, Andreas Fichtner & Heiner Igel

Department of Earth and Environmental Sciences

Ludwig-Maximilians-Universität München

Munich, Germany.

(January 28, 2009)

Running head: **Seismic rotation tomography**

ABSTRACT

We introduce a novel variant of seismic tomography based on collocated measurements of rotational and translational ground motions. This is to assess whether rotations may in the future be incorporated successfully into seismic inverse problems in order to produce better resolved and more realistic tomographic images. Our methodology is based on the definition of the apparent shear wave speed, which is the ratio of the rms velocity and rotation amplitudes. The principal advantages of this definition are (1) that no traveltimes need to be measured and (2) that the apparent shear wave speed is independent from both the source magnitude and the source timing. We derive finite-frequency kernels for the apparent shear wave speed using a combination of the adjoint method and the ray approximation. The properties of these kernels as a function of frequency bandwidth are illustrated and their usefulness for seismic tomography is discussed. In two multi-frequency synthetic inversions we consider a local crosshole tomography and a regional-scale earthquake tomography. Their

results indicate that S wave speed variations can be retrieved accurately from collocated rotation and translation measurements. This suggests that our methodology is a promising extension of conventional seismic tomography.

INTRODUCTION

Highly resolved tomographic images are essential for a variety of applications ranging from global-scale geodynamics to local-scale engineering and exploration. There are two general strategies towards a further improvement of seismic tomography: (1) The development of more elaborate modelling and inversion techniques, such as for example finite-frequency tomography (e.g. Yoshizawa & Kennett, 2004) or nonlinear full waveform inversion (e.g. Fichtner et al., 2008). (2) The incorporation of previously unexploited data such as surface wave amplitudes, exotic phases and measurements of seismically induced strain (e.g. Mikumo & Aki, 1964) or rotations. In this paper we focus on possible improvements of seismic tomography through the incorporation of rotation measurements.

The observation of seismically induced rotational ground motions is becoming increasingly feasible and reliable thanks to the recent developments of high-precision rotation sensors (e.g. Schreiber et al., 2006, 2009). Several authors observed rotations excited by teleseismic waves (e.g. Pancha et al., 2000; Igel et al., 2005, 2007, Cochard et al., 2006). Reports on rotational ground motions recorded in the near-source region may be found in Nigbor (1994), Takeo (1998), Nigbor et al. (2009), Lee et al. (2009), or Wassermann et al. (2009). Seismically induced rotational ground motions contain information about the structure of the Earth: Igel et al. (2005, 2007) and Cochard et al. (2006) inferred local phase velocities from collocated measurements of translations and rotations. Wang et al. (2009) and Stupazzini et al. (2009) used the same amplitude ratio between transverse motion and rotation rate (vertical axis) to identify the low-subsurface velocities associated with sedimentary basin structure. Pham et al. (2009) used rotational signals in the coda of P-waves to constrain crustal scattering. They exploited the fact that rotational motions around the vertical axis are predominantly sensitive to SH-type motions. Based on Full Ray Theory

modelling, Ferreira & Igel (2009) demonstrated a clearly observable effect of near-receiver heterogeneities on rotational motions of Love waves − suggesting that they could be used systematically to infer Earth structure.

A first step towards the solution of structural inverse problems using measurements of rotational ground motions was taken by Fichtner & Igel (2009). They studied the apparent shear wave speed β_a, defined as the ratio of the rms displacement velocity, $||\mathbf{v}||_2$, and the rms rotation amplitude $||\omega||_2$ of a seismic phase or waveform (the measurement time window has to be carefully chosen):

$$\beta_a(\mathbf{x}^r) = \frac{||\mathbf{v}(\mathbf{x}^r)||_2}{||\omega(\mathbf{x}^r)||_2}\,. \tag{1}$$

The symbol $\mathbf{v}(\mathbf{x}^r)$ denotes the displacement velocity at position $\mathbf{x}^r$, ω is the curl of $\mathbf{u}$, i.e. $\omega = \nabla \times \mathbf{u}$, and $||.||_2$ is the L_2 norm.

We list some of the properties of β_a that are particularly interesting in the context of structural inverse problems: (1) No traveltimes need to be measured to determine β_a. (2) For a body S wave in an unbounded and homogeneous medium, β_a is equal to the true S wave speed, i.e. $\beta_a = \beta$. This suggests that β_a contains directly observable information about Earth structure. (3) The apparent shear wave speed, β_a is independent of both the source timing and the source magnitude − two parameters that are often not well constrained. (4) As demonstrated by Fichtner & Igel (2009), the sensitivity of β_a with respect to the true S wave speed, β, is largest in the near-receiver region. This is in contrast to sensitivities for travel times or amplitudes that are nonzero in a volume around the entire ray path (e.g. Dahlen et al., 2000, 2002).

The characteristics of the apparent shear wave speed suggest that it may be used for local tomography with both active or passive sources. Inferring Earth structure from measurements of β_a may be a complement to classical receiver function studies and to local earthquake to-

mography in regions with little or no seismicity. Applications to engineering or exploration problems can equally be envisioned.

In this paper we explore how the apparent shear wave speed, β_a, may be used for the solution of structural inverse problems. Our principal objectives are the development of an efficient tool that allows us to compute sensitivity kernels for β_a measured on body S waves and to use them in synthetic inversions for near-receiver structure.

This paper is organised as follows: We start with the theory needed for the computation of sensitivity kernels using a combination of the adjoint method with the ray approximation. Subsequently, we show sensitivity kernels for β_a measurements in different frequency ranges, and we compare them to the kernels for measurements of the rms velocity and the rms rotation. In the synthetic inversions we focus on applications to local-scale crosshole tomography and regional-scale earthquake tomography.

RAY-THEORETICAL COMPUTATION OF SENSITIVITY KERNELS

Theory

We combine the adjoint method with ray theory to compute sensitivity kernels for β_a. The adjoint method (e.g. Lions, 1968; Tarantola, 1988; Tromp et al., 2005; Fichtner et al., 2006) allows us to avoid the lengthy expressions and approximations of scattering theory that was used for the same purpose by Yomogida & Aki (1987), Yomogida (1992), Dahlen et al. (2000) and Dahlen & Baig (2002). The resulting formulas can be solved efficiently, and they are correct within the well-known validity range of ray theory (e.g. Červený, 2001). This does not impose restrictions in the context of this study because we focus on the direct S wave phase and we generally consider media with sufficiently smooth heterogeneities.

From the quotient rule applied to the definition (1) we deduce that the relative sensitivity density of β_a with respect to β, denoted by $\beta_a^{-1}\delta_\beta\beta_a = \delta_\beta \ln \beta_a$, can be expressed in terms of the sensitivity densities of $||\mathbf{v}||_2$ and $||\omega||_2$:

$$\delta_\beta \ln \beta_a = \delta_\beta \ln ||\mathbf{v}||_2 - \delta_\beta \ln ||\omega||_2 \,. \tag{2}$$

In the interest of notational brevity we omit the dependencies on $\mathbf{x}^r$ wherever possible. The principal result of the adjoint method is that sensitivity densities can be written as a time integral that involves the forward field $\mathbf{u}$ and an adjoint field ψ. In the special case of the sensitivity densities $\delta_\beta \ln ||\mathbf{v}||_2$ and $\delta_\beta \ln ||\omega||_2$ we have

$$\delta_\beta \ln ||\mathbf{v}||_2 = 2\rho\beta^{-1} \int_T \dot{\psi}^v \cdot \mathbf{v} \, dt \,, \tag{3}$$

and

$$\delta_\beta \ln ||\omega||_2 = 2\rho\beta^{-1} \int_T \dot{\psi}^\omega \cdot \mathbf{v} \, dt \,, \tag{4}$$

where ψ^v and ψ^ω denote the adjoint fields corresponding to measurements of $||\mathbf{v}||_2$ and $||\omega||_2$, respectively. We symbolise by T the time interval from the source origin time to the end of the observation. The regular velocity field $\mathbf{v}$ is governed by the elastic wave equation

$$\rho\ddot{\mathbf{u}} - \nabla \cdot (\mathbf{C} : \nabla \mathbf{u}) = \mathbf{f} \,, \tag{5}$$

where the symbols $\mathbf{C}$ and $\mathbf{f}$ denote the fourth-order elastic tensor and an external force density, respectively. The displacement $\mathbf{u}$ and the displacement velocity $\mathbf{v}$ are related through $\mathbf{v} = \dot{\mathbf{u}}$. We omit the visco-elastic dissipation because we found its effect on the shape of sensitivity kernels to be negligible. Both adjoint fields ψ^v and ψ^ω are determined as the solutions of an adjoint wave equation that is equivalent to the regular wave equation (5):

$$\rho\ddot{\psi}^v - \nabla \cdot (\mathbf{C} : \nabla \psi^v) = \mathbf{f}^v \,, \quad \rho\ddot{\psi}^\omega - \nabla \cdot (\mathbf{C} : \nabla \psi^\omega) = \mathbf{f}^\omega \,. \tag{6}$$

The symbols $\mathbf{f}^v$ and $\mathbf{f}^\omega$ are the adjoint sources for ψ^v and ψ^ω, respectively. In contrast to the initial conditions of the regular wave equation, the adjoint wave equations are complemented by homogeneous terminal conditions. They require that the adjoint field be zero at any time after the end of the observation time span (e.g. Tarantola, 1988). As demonstrated by Fichtner and Igel (2009), the components of $\mathbf{f}^v$ and $\mathbf{f}^\omega$ are given by

$$f_i^v(\mathbf{x},t) = ||\dot{\mathbf{u}}(\mathbf{x}^r)||_2^{-2}\, \ddot{u}_i(\mathbf{x}^r,t)\, \delta(\mathbf{x}-\mathbf{x}^r) \tag{7}$$

and

$$f_i^\omega(\mathbf{x},t) = -||\omega(\mathbf{x}^r)||_2^{-2}\, \varepsilon_{ijk}\, \omega_k(\mathbf{x}^r,t)\, \frac{\partial}{\partial x_j}\, \delta(\mathbf{x}-\mathbf{x}^r)\,, \tag{8}$$

where ε_{ijk} denotes the Levi-Civita alternating symbol. Thus, both adjoint sources act at the receiver location $\mathbf{x}^r$ and their temporal evolution is determined by the observed acceleration and rotation fields. Interestingly, $\mathbf{f}^\omega$ corresponds to an anti-symmetric moment tensor source that does not radiate far-field S waves. This highlights the purely mathematical and abstract nature of the adjoint fields and their sources.

Instead of solving the regular wave equation (5) and adjoint equations (6) numerically − as done for example by Fichtner & Igel (2009) − we use the ray-theoretical solutions that are valid in the absence of caustics and strong heterogeneities:

$$\mathbf{u}(\mathbf{x},t) \quad = \mathbf{A}(\mathbf{x})\, s(t - T_s(\mathbf{x}))\,, \tag{9}$$

$$\psi^v(\mathbf{x},t) \quad = \mathbf{A}^v(\mathbf{x})\, s^v(T_r(\mathbf{x}) - t)\,, \tag{10}$$

$$\psi^\omega(\mathbf{x},t) \quad = \mathbf{A}^\omega(\mathbf{x})\, s^\omega(T_r(\mathbf{x}) - t)\,. \tag{11}$$

The vectors $\mathbf{A}$, $\mathbf{A}^v$ and $\mathbf{A}^\omega$ incorporate the amplitudes and polarisations of the different fields while the functions s, s^v and s^ω represent their respective wave forms. The travel time field T_s is measured from the regular source of the forward field, and the travel time field T_r is measured from the receiver. Note that the term $(T_r - t)$ appears in the expressions for ψ^v

and ψ^ω as a consequence of the terminal conditions. We abstain from a detailed discussion of ray theory because it can be found in standard text books (e.g. Červený, 2001; Aki & Richards, 2002). Combining equations (2) to (4) and (9) to (11) yields the following working formula for the computation of the sensitivity density $\delta_\beta \ln \beta_a$ as a function of position $\mathbf{x}$:

$$\delta_\beta \ln \beta_a(\mathbf{x}) = -2\frac{\rho(\mathbf{x})}{\beta(\mathbf{x})}\mathbf{A}(\mathbf{x}) \tag{12}$$

$$\cdot \left[\mathbf{A}^v(\mathbf{x}) \int \dot{s}^v(T_r(\mathbf{x}) - t)\, \dot{s}(t - T_s(\mathbf{x}))\, dt - \mathbf{A}^\omega(\mathbf{x}) \int \dot{s}^\omega(T_r(\mathbf{x}) - t)\, \dot{s}(t - T_s(\mathbf{x}))\, dt\right] . \tag{13}$$

Equation (12) suggests a simple computational recipe for the computation of the sensitivity kernels $\delta_\beta \ln \beta_a$: 1) Compute the ray-theoretical solution (9) of the regular wave field $\mathbf{u}$, travelling from the source to the receiver. 2) Use this solution to determine the adjoint sources (7) and (8). 3) Compute the regular wave field plus the adjoint wave fields (10) and (11) at a point $\mathbf{x}$ in space by solving the ray tracing and dynamic ray tracing equations. 4) Assemble the sensitivity kernel according to equation (12).

Examples

We illustrate the computation of sensitivity kernels for a medium with a linear velocity gradient from $\beta = 3.2$ km/s at the surface to $\beta = 5.5$ km/s at 350 km depth (figure 1). The sensitivities of the rms rotation, $\delta_\beta \ln ||\omega||_2$ and the rms velocity, $\delta_\beta \ln ||\mathbf{v}||_2$, both exhibit a well-known dependence on the frequency band width of the signal. Comparatively narrow frequency bands generate broad kernels with significant contributions at larger distances from the geometric ray path. As the bandwidth increases, the kernels become successively narrower and stronger in amplitude. This effect is visualised in the different columns of figure 1, where the frequency bandwidth increases from 0.3 Hz (left column) to 2.5 Hz (right column). Visually, the kernels $\delta_\beta \ln ||\omega||_2$ and $\delta_\beta \ln ||\mathbf{v}||_2$ are hardly distinguishable. However,

their differences become apparent in the kernel for the apparent shear wave speed, $\delta_\beta \ln \beta_a$, computed − according to equation (2) − as the difference $\delta_\beta \ln \beta_a = \delta_\beta \ln ||\mathbf{v}||_2 - \delta_\beta \ln ||\omega||_2$. The β_a kernels in the bottom row of figure 1 reveal some general characteristics, already discussed by Fichtner & Igel (2009): The sensitivity decreases with increasing distance from the receiver, the only exception being the immediate vicinity of the source where all kernels are singular. In the first Fresnel zone the sensitivity is comparatively small, whereas it remains large in the higher Fresnel zones near the receiver. The regions of high sensitivity of the β_a kernel occupy less space than in the kernels for rotation amplitudes, velocity amplitudes or finite-frequency traveltimes (Dahlen et al., 2000). This suggests that measurements of the apparent shear wave speed, β_a, may be used to infer small-scale structure especially in the near-receiver region.

FIGURE 1 HERE

SYNTHETIC INVERSIONS

In the following paragraphs, we give two examples of synthetic inversions with β_a measurements: a local crosshole tomography and a regional earthquake tomography. This is to illustrate the possible range of applicability of our approach. To obtain optimal results, we employ a nonlinear optimisation scheme with a successively increasing frequency bandwidth.

We denote by $\beta^0_{a,i}$ and $\beta_{a,i}$ the apparent shear wave speeds for the reference S wave model $\beta^0(\mathbf{x})$, and for the perturbed model $\beta^0(\mathbf{x}) + \delta\beta(\mathbf{x})$, respectively. The subscript i refers to different source and receiver locations, different frequencies or combinations of them. In

the interest of simplicity, we henceforth refer to $\beta_{a,i}$ and $\beta^0_{a,i}$ as *data* and *synthetics*, keeping in mind that the following examples are synthetic inversions. We wish to recover the perturbation $\delta\mathbf{m}$ through the minimisation of the least-squares misfit functional

$$E = \frac{1}{2}\sum_{i=1}^{n}(\beta_{a,i} - \beta^0_{a,i})^2 \,. \tag{14}$$

The Earth model is parameterised by a set of N basis functions, $h_k(\mathbf{x})$, $k = 1, ..., N$. They allow us to express the S wave speed model, $\beta(\mathbf{x})$ as $\beta(\mathbf{x}) = \sum_{k=1}^{N} \beta_k h_k(\mathbf{x})$, where the β_k are scalar parameters. In the interest of simplicity, we choose the basis functions to be cubic blocks. The derivative of the objective function E with respect to the coefficients β_k is now given by the projection of the sensitivity kernel $\delta_\beta\beta_{a,i}(\mathbf{x})$ onto the basis function h_k:

$$\frac{\partial E}{\partial \beta_k} = \sum_{i=1}^{n}(\beta_{a,i} - \beta^0_{a,i}) \int_G h_k(\mathbf{x})\, \delta_\beta\beta_{a,i}(\mathbf{x})\, d^3\mathbf{x}\,, \quad k = 1, ..., N\,. \tag{15}$$

The symbol G denotes the volume of the Earth model. For multiple source/receiver geometries the total gradient is equal to the weighted sum of the single-source/single-receiver gradients, where the weights are the residuals $\beta_{a,i} - \beta^0_{a,i}$. Using the derivatives E, we iteratively minimise the misfit with a preconditioned steepest descent algorithm. The preconditioner tapers the singularity of the sensitivity kernels directly at the receiver. It thus prevents the minimisation scheme from converging towards a local minimum where all heterogeneities are concentrated at the receiver locations. In the course of the iterative misfit minimisation we successively increase the frequency content. This allows us to ensure the quasi-linearity of the misfit functional with respect to Earth model perturbations.

Scenario I: Local-scale crosshole tomography

Crosshole tomography is a standard tool used to infer small-scale structures that are relevant in engineering and exploration applications (e.g. Angioni et al., 2003; Wong, 2000)

and in studies of local tectonics (Bleibinhaus et al., 2007). In our first example, visualised in the left panel of figure 2, we consider two 80 m deep boreholes at a distance of 80 m. Eight seismic sources at 5 to 75 m depth generate S waveforms recorded at 70 equally spaced receivers between 5 and 75 m depth. In the course of the iteration we successively use the following frequency bands: 0.1 - 0.6 kHz, 0.1 - 0.9 kHz, 0.1 - 1.2 kHz, 0.1 - 1.5 kHz and 0.1 - 1.8 kHz. The target model that we wish to invert for consists of two high-velocity perturbations and a low-velocity perturbation superimposed on a homogeneous background S velocity of 2 km/s. They represent strong changes of the medium properties in the shallow subsurface. To comply with the requirements of ray theory, used to compute waveforms and sensitivity kernels, we choose the perturbations to be smooth. They are similar in complexity to synthetic structures chosen by various authors (e.g. Zhou et al., 2008; Linde et al., 2008).

The fictitious data set used for the synthetic tomography contains 40 different recording series (eight sources, five frequencies), a collection of which is shown in figure 3. While interpretations of β_a should be done with caution, we note that the strength of β_a variations is proportional to the frequency bandwidth. Moreover, data produced by sources close to the perturbations (right panel of figure 3) give a hint to changes between high- and low-velocity zones as well as to the perturbation intensities.

The inversion starts with a misfit minimisation for a homogeneous initial model and the smallest frequency band from 0.1 - 0.6 kHz. After seven iterations the synthetics reproduce the observations well (figure 4), and the resulting image can be used as initial model for the inversion in the next higher frequency band. We repeat this procedure until we reach the fifth frequency band (0.1 - 1.8 kHz). The final model is presented in the right panel of figure 2.

The inversion result localises low- and high-velocity zones correctly. The shapes and the intensities of the perturbations are similar to the original model. Small differences in the shape of the perturbations remain. They may be attributed to an imperfect data coverage. We note that this example is a proof of concept and not a systematic resolution study that would need to be performed for each specific application.

FIGURES 2, 3 & 4 HERE

Scenario II: Regional-scale earthquake tomography

The purpose of the second example is to show that our method is as well applicable to regional-scale tomography problems. For this we mimic an earthquake tomography across a subduction zone, as performed for example in the Southern Andes (Bohm et al., 2002) or Central America (Syracuse et al., 2008). Inferring structural heterogeneity in tectonically active zones is essential for studies of the Earth's dynamics (e.g. Schuberth et al., 2009). The target model, shown in the left panel of figure 5, contains a -1 km/s low velocity region that represents a zone of subduction-related melt ascent. This is flanked by two $+1$ km/s high velocity regions. The background velocity is 4.5 km/s.

The seismic experiment includes six earthquake sources located regularly along a fictitious downgoing plate at depths between 80 km and 200 km. 120 receiver stations are equally spaced in a surface profile of 238 km length. The frequency bands for the inversion are 0.1-1.0 Hz, 0.1-1.5 Hz and 0.1-2.0 Hz. They provide a data set of 18 different recording series (six sources, three frequencies). In figure 6 data curves are plotted for all frequency bands and sources at the profile locations $x = 100$ km, $x = 180$ km and $x = 260$ km. An ad

hoc interpretation of data plots is restricted to the same level as in the first example. Also the inversion principle is analogous to the description in scenario I.

Figure 7 reproduces the minimisation of the data misfit between data and synthetics for the smallest frequency band in nine iteration steps. The inversion result (figure 5, right panel) highlights clearly the main characteristics of the subduction zone model. Nevertheless, some artefacts appear especially in source regions. This may be a consequence of the singularity of the β_a kernels directly at the source locations.

FIGURES 5, 6 & 7 HERE

DISCUSSION

We presented a novel variant of seismic tomography based on collocated measurements of translational and rotational ground motions. For the iterative solution of the inverse problem we combined the adjoint method and the ray approximation. The use of ray theory was motivated by its low computational costs that allow us to perform a large number of numerical experiments, and thus to gain intuitive understanding of inverse problems that involve measurements of the apparent shear wave speed, β_a. While being numerically efficient, the limitations of ray theory restricted this study to smooth models and high-frequency S waves. This may be improved in future applications by fully numerical wave propagation schemes that allow us to include lower frequencies and any type of seismic wave.

The measurement of the apparent shear wave speed is attractive because it is independent of both the source timing and the source magnitude. This simplifies the combined source/structure inverse problem. Moreover, no arrival times need to be measured. In fact,

fully numerical wave propagation in principle allows us to use any part of a seismogram for β_a measurements (Fichtner & Igel, 2009).

A disadvantage of the proposed method lies in the difficulty of measuring both the amplitudes of translational and rotational ground motions with high precision. While the synthetic inversions in the previous paragraphs have clearly shown that β_a measurements allow us to obtain well-resolved tomographic images, the variations of β_a induced by yet undiscovered Earth structure may be difficult to identify. A detailed analysis of β_a variations is work in progress.

CONCLUSIONS & OUTLOOK

The principal objective of this study was to assess whether measurements of seismically induced rotational ground motions may in the future be incorporated successfully into seismic inverse problems in order to produce better resolved and more realistic tomographic images. From the synthetic tests presented in the previous paragraphs we conclude that collocated displacement and rotation measurements, combined to the apparent shear wave speed β_a, indeed do have this potential. Some of the next steps to be taken are (1) the extraction of structural information from real data measurements of β_a, (2) the transition from ray theory to fully numerical wave propagation, (3) the incorporation of more seismic phases and surface waves, (4) the performance of systematic resolution analyses and (5) the comparison with standard tomographic methods. It is important to note that the applicability of the porposed method rests on the availability of more data and the further development and improvement of appropriate sensor technology.

ACKNOWLEDGEMENTS

The authors wish to thank the members of the Munich seismology group for many critical and fruitful discussions. This study would not have been possible without the technical support provided by Jens Oeser.

REFERENCES

[1] Aki, K., Richards, P. G., 2002, Quantitative seismology, 2nd edition: University Science Books.

[2] Angioni, T., Rechtien, R. D., Cardimona, S. J., Luna, R., 2003, Crosshole seismic tomography and borehole logging for engineering site characterization in Sikeston, MO, USA: Tectonophysics, **368**, 119-137.

[3] Bleibinhaus, F., Hole, J. A., Ryberg, T., Fuis, G. S., 2007, Structure of the California Coast Ranges and San Andreas Fault at SAFOD from seismic waveform inversion and reflection imaging: J. Geophys. Res., **112**, B06315.

[4] Bohm, M., Lüth, S., Echtler, H., Asch, G., Bataille, K., Bruhn, C., Rietbrock, A., Wigger, P., 2002, The Southern Andes between 36^o and 40^o latitude: seismicity and average seismic velocities: Tectonophysics, **356**, 275-289.

[5] Červený, V., 2001, Seismic ray theory: Cambridge University Press.

[6] Cochard, A., Igel, H., Schuberth, B., Suryanto, W., Velikoseltsev, A., Schreiber, U., Wassermann, J., Scherbaum, F., Vollmer, D., 2006, Rotational motions in seismology: theory, observation, simulation. In: Earthquake Source Asymmetry, Structural Media and Rotation Effects, R. Teisseyre, M. Takeo, and E. Majewski (Editors), p. 391-411, Springer Verlag, Heidelberg.

[7] Dahlen, F. A., Hung, S.-H., Nolet, G., 2000, Fréchet kernels for finite-frequency travel times - I. Theory: Geophys. J. Int., **141**, 157-174.

[8] Dahlen, F. A., Baig, A. M., 2002, Fréchet kernels for body-wave amplitudes: Geophys. J. Int., **150**, 440-466.

[9] Ferreira, A. M. G., Igel, H., 2009, Rotational motions of seismic surface waves in a laterally heterogeneous Earth: Bull. Seis. Soc. Am., in press.

[10] Fichtner, A., Bunge, H.-P., Igel, H., 2006, The adjoint method in seismology I: theory: Phys. Earth Planet. Int., **157**, 86-104.

[11] Fichtner, A., Kennett, B. L. N., Igel, H., Bunge, H.-P., 2008, Theoretical background for continental and global scale full-waveform inversion in the time-frequency domain: Geophys. J. Int., **175**, 665-685.

[12] Fichtner, A., Igel, H., 2009, Sensitivity densities for rotational ground motion measurements: Bull. Seis. Soc. Amer., **99**, in press.

[13] Igel, H., Schreiber, U., Flaws, A., Schuberth, B., Velikoseltsev, A., Cochard, A., 2005, Rotational motions induced by the M 8.1 Tokachi-oki earthquake, September 25, 2003: Geophys. Res. Lett., **32**, L08309.

[14] Igel, H., Cochard, A., Wassermann, J., Flaws, A., Schreiber, U., Velikoseltsev, A., Dinh, N. P., 2007, Broad-band observations of earthquake-induced rotational ground motions: Geophys. J. Int., **168**, 182-197.

[15] Lee, W. H. K., Huang, B. S. , Langston, C. A. , Lin, C. J. , Liu, C. C., Shin, T. C., Teng, T. L., Wu, C. F. (2009b). Review: Progress in rotational ground-motion observations from explosions and local earthquakes in Taiwan: Bull. Seis. Soc. Amer., **99**, in press.

[16] Linde, N., Tryggvason, A., Peterson, J. E., Hubbard, S. S., 2008, Joint inversion of crosshole radar and seismic traveltimes acquired at the South Oyster bacterial transport site: Geophysics, **73**, G29-G37.

[17] Lions, J. L., 1968, Contrôle optimal de systèmes gouvernés par des équations aux dérivées partielles: Dunod Gauthier-Villars.

[18] Mikumo, T., Aki, K., 1964, Determination of local phase velocity by intercomparison of seismograms from strain and pendulum instruments. J. Geophys. Res., **69**, 721-731.

[19] Nigbor, R. L., 1994, Six-degree-of-freedom ground motion measurement. Bull. Seismol. Soc. Am., **84**, 1665-1669.

[20] Nigbor, R. L., Evans, J. R., Hutt, C. R., 2009, Laboratory and field testing of commercial rotational seismometers: Bull. Seis. Soc. Amer., **99**, in press.

[21] Pancha, A., Webb, T. H., Stedman, G. E., McLeod, D. P., Schreiber, K. U., 2000, Ring laser detection of rotations from teleseismic waves: Geophys. Res. Lett., **27**(21), 3553-3556.

[22] Pham, N. D., Igel, H., Wassermann, J., Käser, M., de la Puente, J., Schreiber, U., 2009, Observations and modeling of rotational signals in the P-coda: Constraints on crustal scattering: Bull. Seis. Soc. Amer., **99**, in press.

[23] Schreiber, U., Stedman, G. E., Igel, H., Flaws, A., 2006, Ring laser gyroscopes as rotation sensors for seismic wave studies: In: Earthquake Source Asymmetry, Structural Media and Rotation Effects, Springer, New York.

[24] Schreiber, K. U., Hautmann, J. N., Velikoseltsev, A., Wassermann, J., Igel, H., Otero, J., Vernon, F., Wells, J.-P. R., 2009, Ring laser measurements of ground rotation for seismology: Bull. Seis. Soc. Amer., **99**, in press.

[25] Schuberth, B., Bunge, H.-P., Steinle-Neumann, G., Moder, C., Oeser, J., 2009, Thermal versus elastic heterogeneity in high-resolution mantle circulation models with pyrolite

composition: High plume excess temperatures in the lowermost mantle: Geochemistry Geophysics Geosystems, **10**, Q01W01, doi:10.1029/2008GC002235.

[26] Stupazzini, M., de la Puente, J., Smerzini, C., Käser, M., Igel, H., Castellani, A., 2009, Study of rotational ground motion in the near-field region, **99**, in press.

[27] Syracuse, E. M., Abers, G. A., Fischer, K., Mackenzie, L., Rychert, C., Protti, M., Gonzáles, V., Strauch, W., 2008: Seismic tomography and earthquake locations in the Nicaraguan and Costa Rican upper mantle: Geochem. Geophys. Geosys., **9**(7), Q07S08, doi:10.1029/2008GC001963.

[28] Takeo, M., 1998, Ground rotational motions recorded in near-source region of earthquakes: Geophys. Res. Lett., **25**, 789-792.

[29] Tarantola, A., 1988, Theoretical background for the inversion of seismic waveforms, including elasticity and attenuation: Pure Appl. Geophys., **128**, 365-399.

[30] Tromp, J., Tape, C., Lui, Q., 2005, Seismic tomography, adjoint methods, time reversal and banana-doughnut kernels: Geophys. J. Int., **160**, 195-216.

[31] Wang, H., Igel, H., Gallovic, F., Cochard, A., 2009, Source and basin effects on rotational ground motions: Comparison with translations: Bull. Seis. Soc. Amer., **99**, in press.

[32] Wassermann, J., Lehndorfer, S., Igel, H., Schreiber, U., 2009, Performance test of a commercial rotational motions sensor: Bull. Seis. Soc. Amer., **99**, in press.

[33] Wong, J., 2000, Crosshole seismic imaging for sulfide orebody delineation near Sudbury, Ontario, Canada: Geophysics, **65**(6), 1900-1907.

[34] Yomogida, K., Aki, K., 1987, Amplitude and phase data inversions for phase velocity anomalies in the Pacific Ocean basin: Geophys. J. R. astr. Soc., **88**, 161-204.

[35] Yomogida, K., 1992, Fresnel zone inversion for lateral heterogeneities in the Earth: Pure Appl. Geophys.,**138**(3), 391-406.

[36] Yoshizawa, K., Kennett, B. L. N., 2004, Multimode surface wave tomography for the Australian region using a three-stage approach incorporating finite frequency effects: J. Geophys. Res., **109**, doi: 10.1029/2002JB002254.

[37] Zhou, B. Greenhalgh, S., Green, A., 2008, Nonlinear traveltime inversion scheme for crosshole seismic tomography in tilted transversely isotropic media: Geophysics, **73**, D17-D33.

FIGURES

Figure 1: Finite-frequency kernel gallery for rms amplitude, rms rotation and apparent shear wave speed measurements.

Figure 2: Target model and inverted model for the synthetic crosshole tomography.

Figure 3: Relative variations of the apparent shear wave speed in the crosshole synthetic inversion. Plots are for different depths and frequency bands.

Figure 4: Development of the misfit in the course of the multi-frequency inversion in the crosshole synthetic tomography.

Figure 5: Target model and inverted model for the synthetic regional earthquake tomography.

Figure 6: Relative variations of the apparent shear wave speed in the synthetic earthquake tomography. Plots are for different frequency bands and positions along the receiver line.

Figure 7: Development of the misfit in the course of the multi-frequency inversion in the synthetic earthquake tomography.

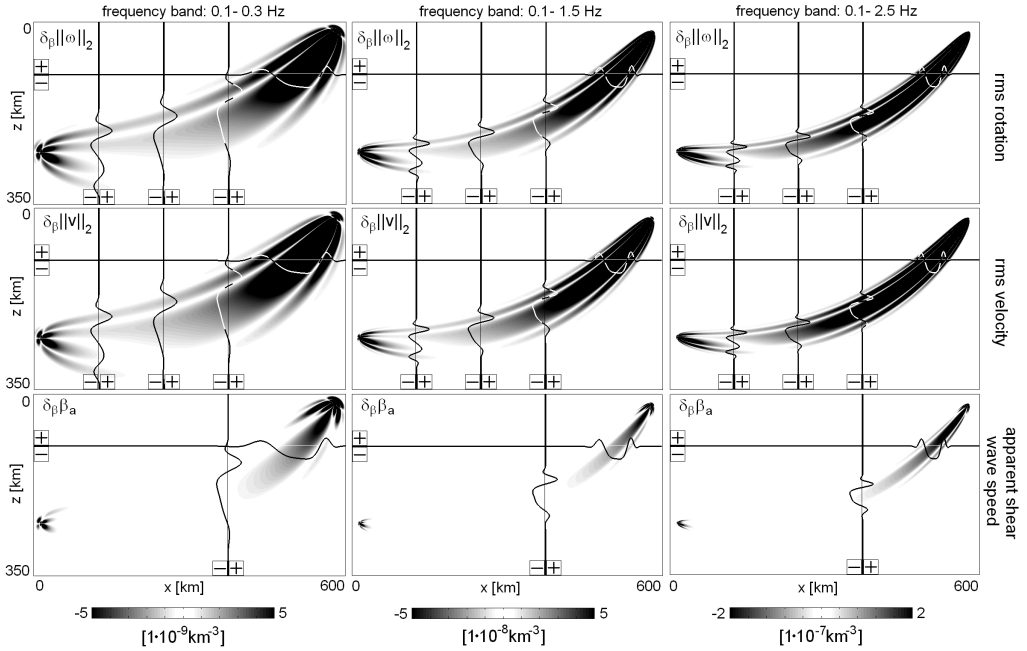

Figure 1: Sensitivity kernels for the rms rotation, $||\omega||_2$ (top row), the rms velocity, $||\mathbf{v}||_2$ (middle row) and the apparent shear wave speed, β_a (bottom row). The columns correspond to different frequency bandwidths of the recorded velocity waveform: $0 - 0.3$ Hz (left), $0 - 1.5$ Hz (middle) and $0 - 2.5$ Hz (right). Superimposed curves are normalised cuts through the sensitivity kernels in horizontal and vertical directions. All sensitivities are with respect to the S wave speed, β. The source is at 250 km depth and the receiver is near the surface.

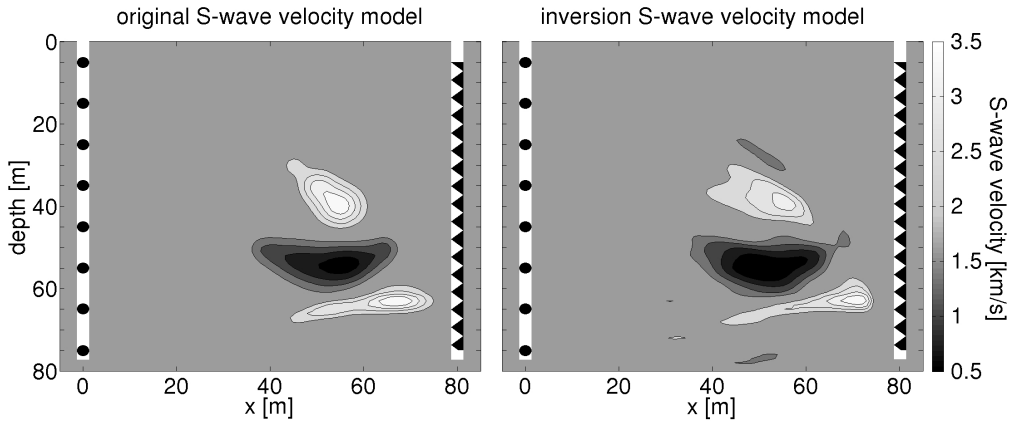

Figure 2: Left: Crosshole tomography scenario with two 80 m deep boreholes (vertical white columns) at 80m distance. Sources and receivers are equally spaced between 5 and 75 m depth. The right borehole contains 70 receivers (black sawtooth line) recording the signals from eight sources (black bullets) in the left borehole. The synthetic model contains low- and high-speed variations on a constant S velocity background of 2 km/s. Right: Final model after inversion in the successively broader frequency bands. The original model on the left is well reproduced.

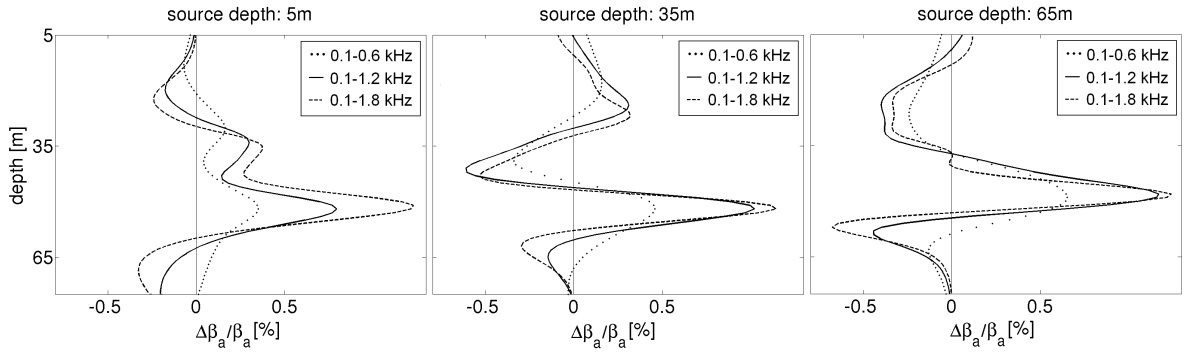

Figure 3: Relative variations of the apparent S wave speed, $\Delta\beta_a/\beta_a$, for seismic sources at 5 m (left), 35 m (middle) and 65 m (right) depth and the following frequency bands: 0.1 - 0.6 kHz (dotted line), 0.1 - 1.2 kHz (solid line) and 0.1 - 1.8 kHz (dashed line).

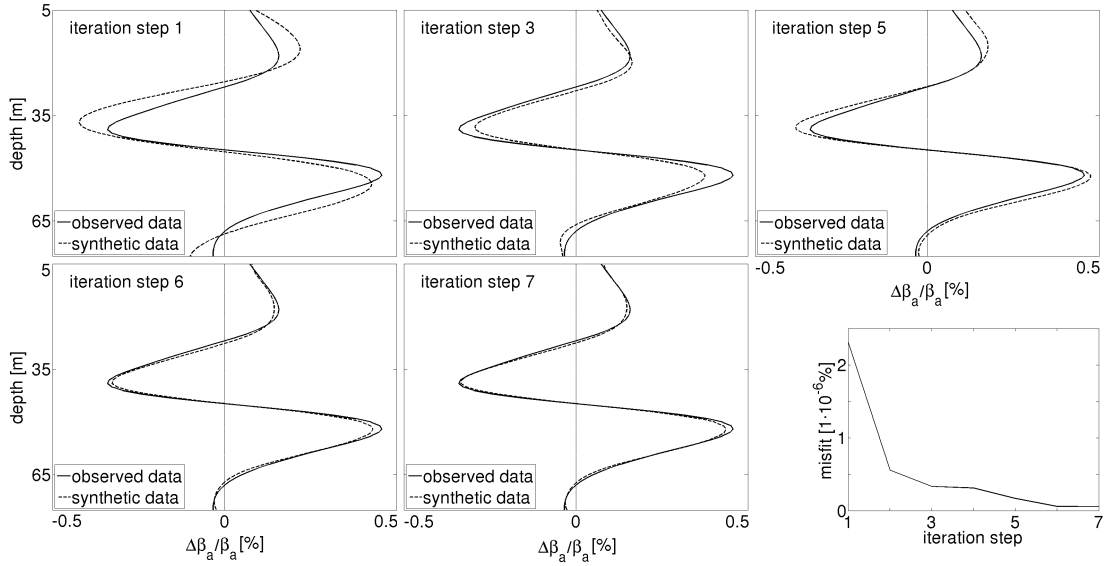

Figure 4: Misfit optimisation between observed and synthetic data in seven iteration steps applied to the data set produced by a source at 5 m depth and the frequency band 0.1 - 0.6 kHz. Data and synthetics match well after seven iterations.

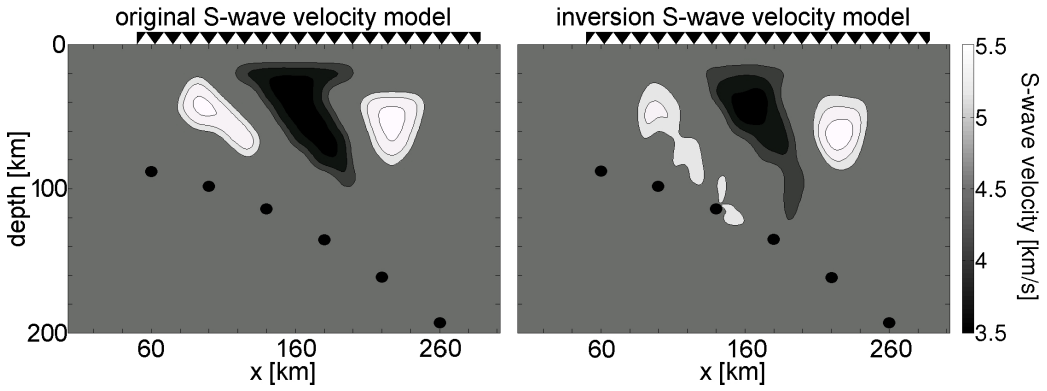

Figure 5: Left: Typical subduction scenario with a low-speed region, caused by melting processes, and two surrounding high-speed zones. Along the downgoing plate six earthquake sources (black bullets) located regularly at depths between 80 km and 200 km yield seismic signals. The black triangles symbolise a receiver profile on the surface with 120 recording stations. Right: Inversion model including six sources, 120 receivers and three frequency bands. The figure shows that the inversion approach combining translational and rotational measurements is well usable for regional-scale tomography.

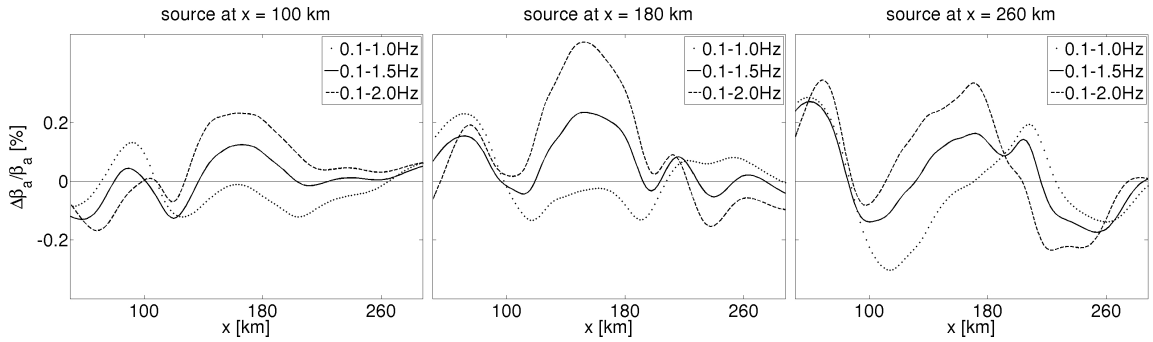

Figure 6: Relative variations of the apparent S wave speed, $\Delta\beta_a/\beta_a$, for three different earthquake sources. In the left panel the source is located at $x = 100$ km, depth $= 96$ km, in the middle panel at $x = 180$ km, depth $= 134$ km and in the right panel the source is at $x = 260$ km, depth $= 192$ km. The data curves represent the following frequency bands: $0.1 - 1.0$ Hz (dotted line), 0.1-1.5 Hz (solid line) and 0.1-2.0 Hz (dashed line).

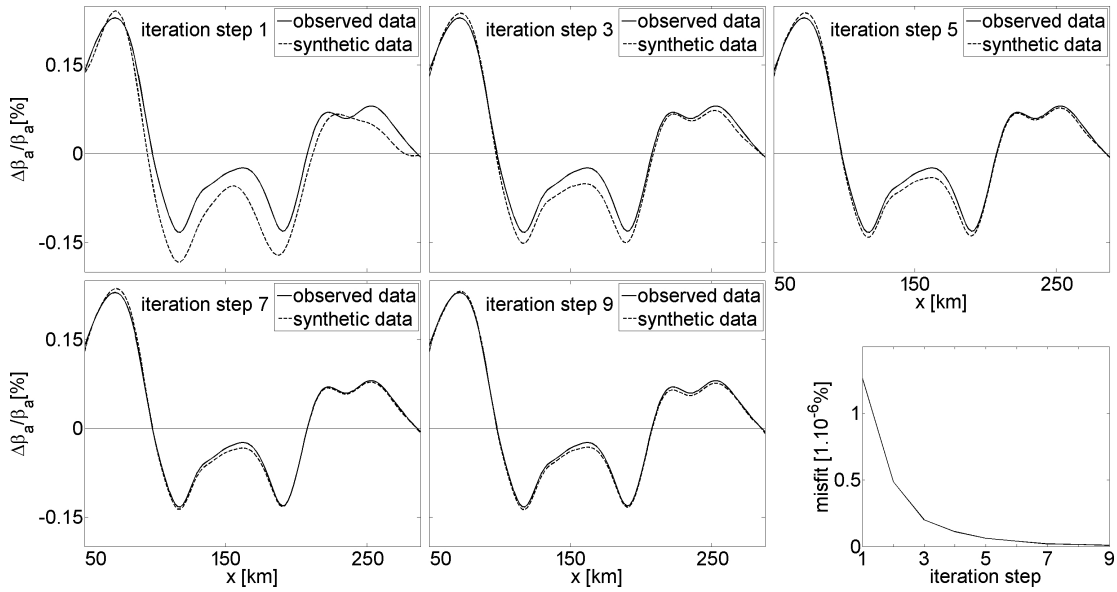

Figure 7: Misfit optimisation between observed and synthetic data. The data curve is produced by an earthquake source at $x = 180$ km, depth = 134 km and by the frequency band 0.1-1.0 Hz. After nine iterations data and synthetics match well.